

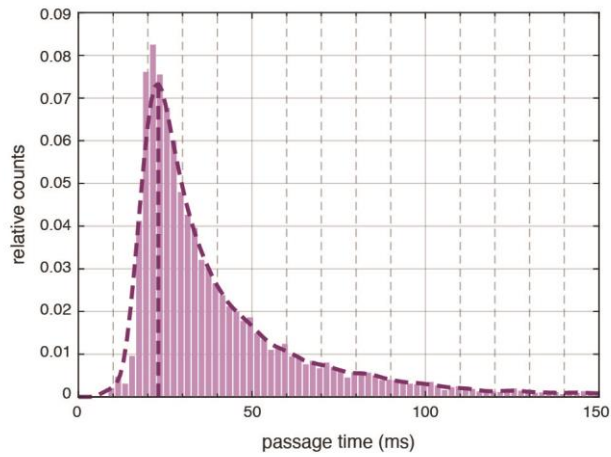
In the format provided by the authors and unedited.

# A comparison of microfluidic methods for high-throughput cell deformability measurements

Marta Urbanska <sup>1,10</sup>, Hector E. Muñoz <sup>2,10</sup>, Josephine Shaw Bagnall <sup>3</sup>, Oliver Otto <sup>1,4</sup>,  
Scott R. Manalis <sup>3,5,6</sup> ✉, Dino Di Carlo <sup>2,7,8</sup> ✉ and Jochen Guck <sup>1,9</sup> ✉

---

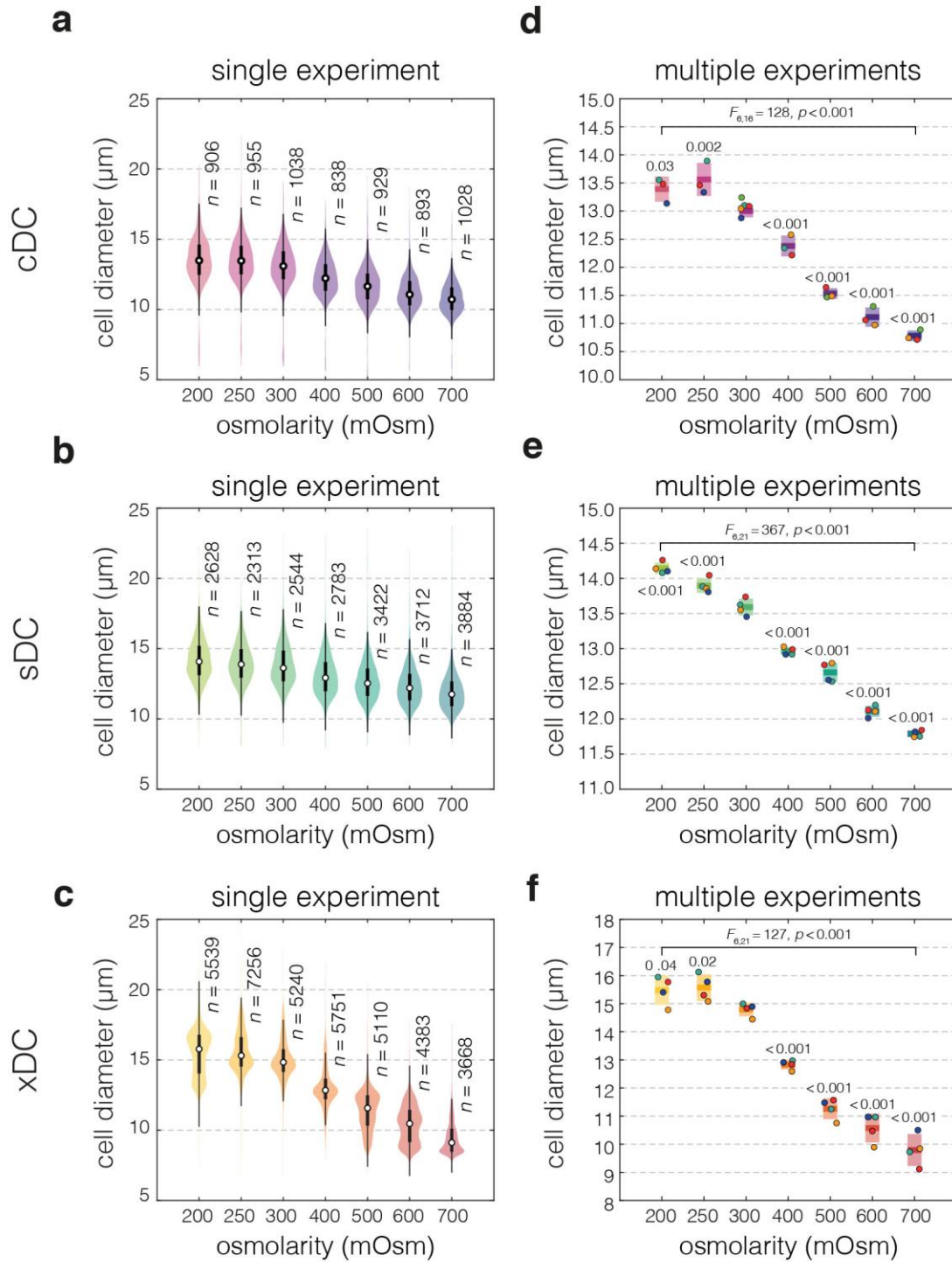
<sup>1</sup>Biotechnology Center, Center for Molecular and Cellular Bioengineering, Technische Universität Dresden, Dresden, Germany. <sup>2</sup>Department of Bioengineering, University of California, Los Angeles, Los Angeles, CA, USA. <sup>3</sup>Department of Biological Engineering, Massachusetts Institute of Technology, Cambridge, MA, USA. <sup>4</sup>Zentrum für Innovationskompetenz: Humorale Immunreaktionen in kardiovaskulären Erkrankungen, Universität Greifswald, Greifswald, Germany. <sup>5</sup>Department of Mechanical Engineering, Massachusetts Institute of Technology, Cambridge, MA, USA. <sup>6</sup>Koch Institute for Integrative Cancer Research, Massachusetts Institute of Technology, Cambridge, MA, USA. <sup>7</sup>California NanoSystems Institute, University of California, Los Angeles, Los Angeles, CA, USA. <sup>8</sup>Jonsson Comprehensive Cancer Center, University of California, Los Angeles, Los Angeles, CA, USA. <sup>9</sup>Max Planck Institute for the Science of Light and Max-Planck-Zentrum für Physik und Medizin, Erlangen, Germany. <sup>10</sup>These authors contributed equally: Marta Urbanska, Hector E. Muñoz. ✉e-mail: [srm@mit.edu](mailto:srm@mit.edu); [dicarlo@ucla.edu](mailto:dicarlo@ucla.edu); [jochen.guck@mpl.mpg.de](mailto:jochen.guck@mpl.mpg.de)



### Supplementary Figure 1

#### Distribution of passage times measured with cDC for untreated HL60 cells.

Bars represent binned data of control HL60 cells pulled from 10 experiments (total cell number,  $n = 9,734$ ). Dashed curve represents Kernel density estimation (KDE) of probability distribution with vertical line at the most represented value equal to 23 ms.

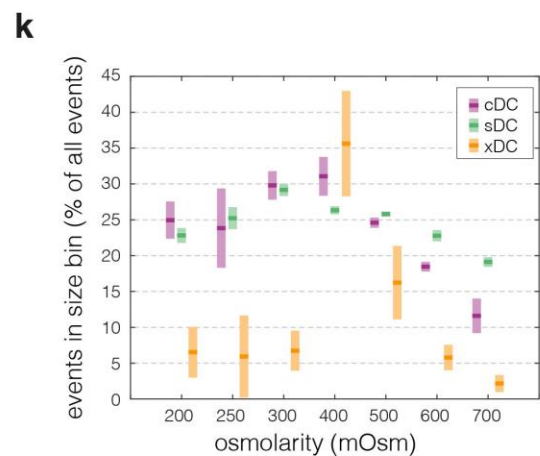
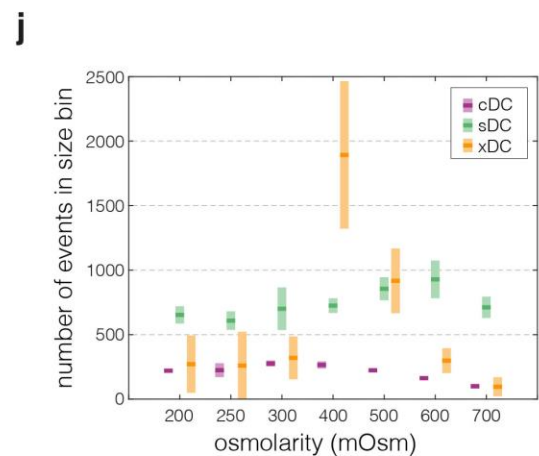
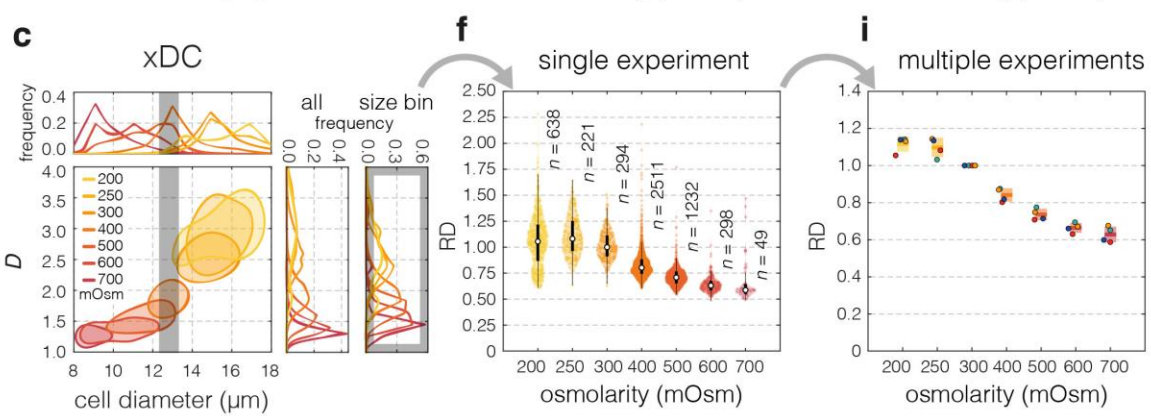
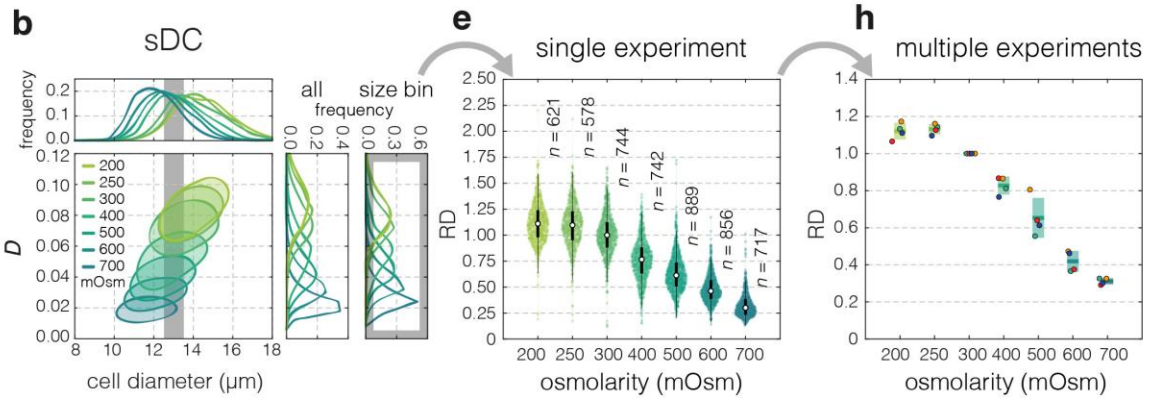
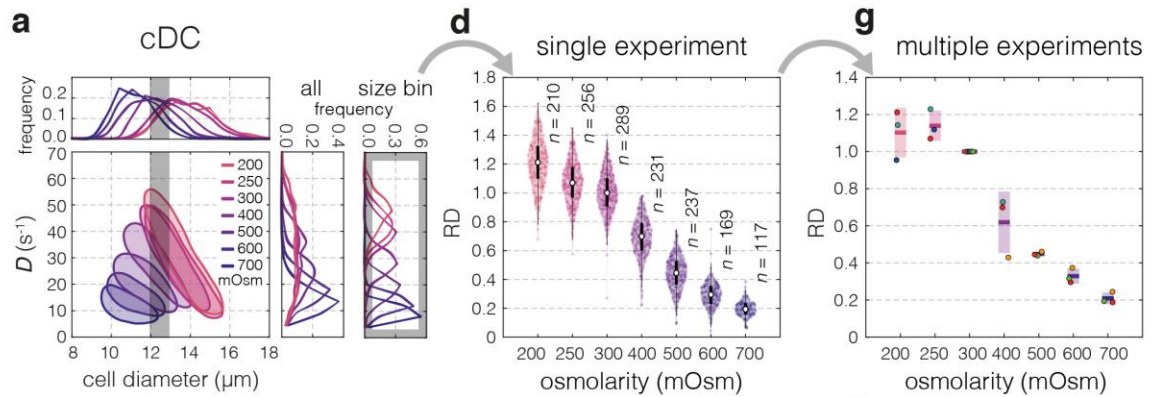


**Supplementary Figure 2**

**Cell diameter of HL60 cells exposed to different osmotic shock conditions.**

(a–c) Violin plots of cell diameter in a single experiment as measured by cDC (a), sDC (b) and xDC (c). Black boxes extend from 25th to 75th percentiles, with a dot at the median, whiskers indicate 1.5× IQR (interquartile range). (d–f) Summary of median cell diameter values obtained in all experiment series with cDC (d), sDC (e) and xDC (f). Data

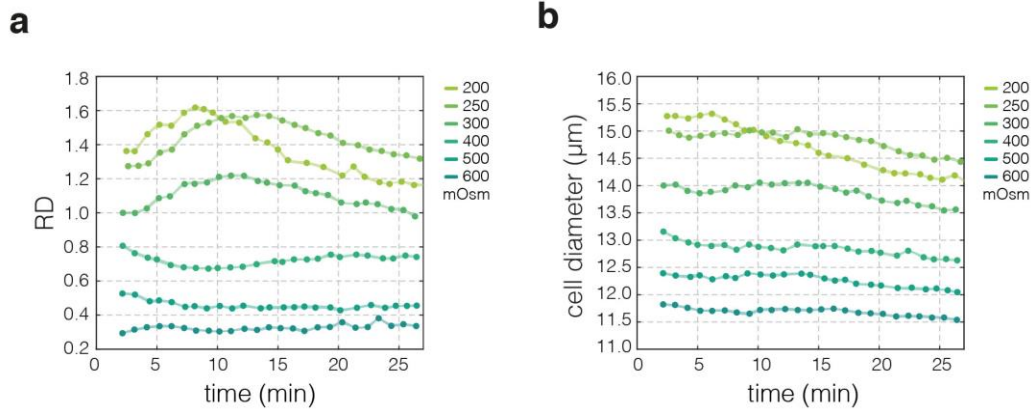
points correspond to medians of individual experiments ( $n = 3, 4$  and  $4$ , for cDC, sDC and xDC, respectively). Conditions measured in the same experimental series are color-coded. Boxes span  $2\times$  standard deviation with a line at the mean of all medians. In (d–f) statistical significance of overall differences among mean cell sizes at different osmolarities was tested using analysis of variance (ANOVA) and its result is shown on top of the horizontal line overarching all conditions. The  $P$  values reported above each box come from comparison of the given treatment to the control condition (300 mOsm) obtained through post-hoc analysis using two-sided pairwise  $t$ -tests for multiple comparison with Benjamin-Hochberg  $P$ -value adjustment.



### Supplementary Figure 3

#### Visualization of bin selection and data processing for osmolarity experiments.

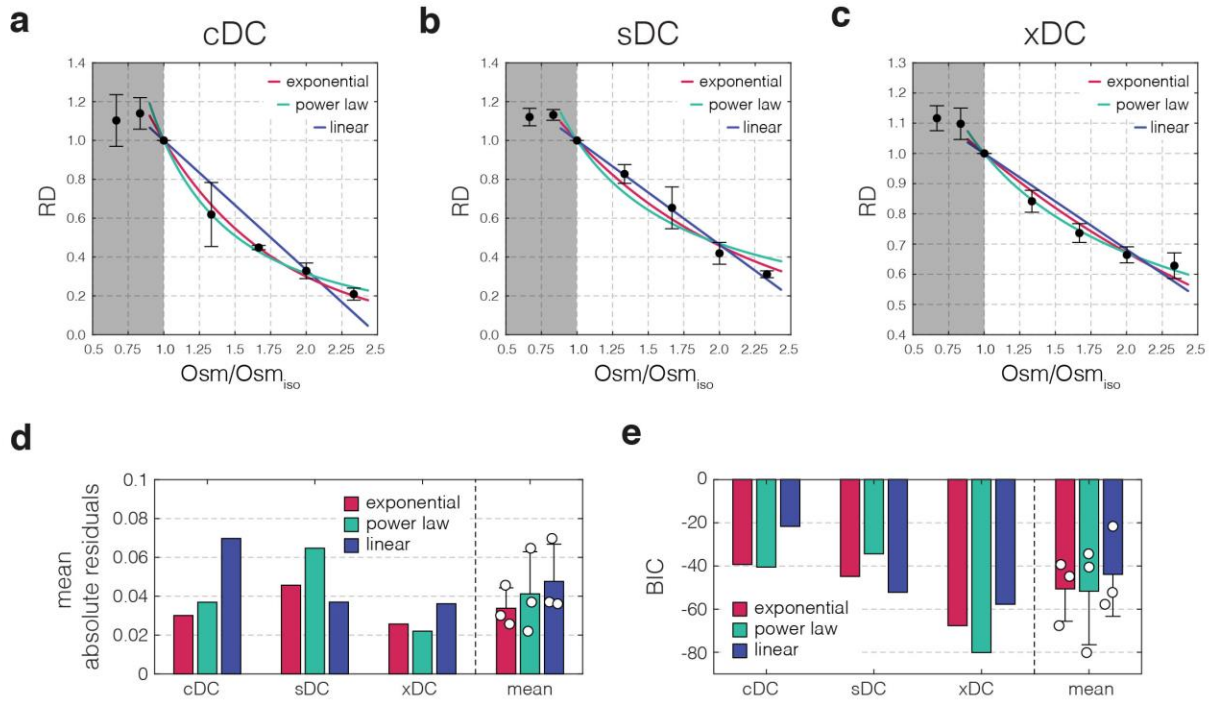
(a–c) 50%-density contour plots of deformability vs cell diameter for an exemplary experiment on HL60 cells subjected to different osmolarity conditions. The contour plots are accompanied by deformability and cell diameter histograms for cDC (a), sDC (b), and xDC (c). The most represented 1- $\mu\text{m}$  wide diameter bins used for relative deformability, RD, calculations and the corresponding deformability histograms are outlined in grey. (d–f) Jitter plots showing distribution of RD from cDC (d), sDC (e), and xDC (f) measurements for a single experiment. Boxes extend from 25th to 75th percentiles, with a dot at the median, whiskers indicate 1.5 $\times$  IQR (interquartile range) and each data point corresponds to an individual cell. (g–i) Summary of RD values obtained in all experimental series with cDC (g), sDC (h) and xDC (i). Data points correspond to medians of every experiment and conditions measured in same experimental series are color-coded. Boxes span 2 $\times$  standard deviation with a line at the mean of all medians. (j) Number of events in the selected 1- $\mu\text{m}$  wide diameter bin for each condition and method. (k) Events selected within the 1- $\mu\text{m}$  wide diameter bin as a percentage of all events measured. In j and k, the boxes span 2 $\times$  standard deviation with a line at the mean. In g–k, the statistics have been calculated for  $n = 3, 4$  and 4 independent measurement replicates, for cDC, sDC and xDC, respectively.



#### Supplementary Figure 4

##### Time-resolved effect of osmotic shock on HL60 deformability and size as measured by sDC.

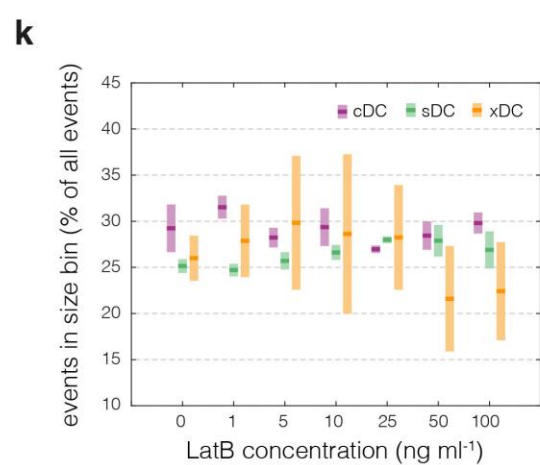
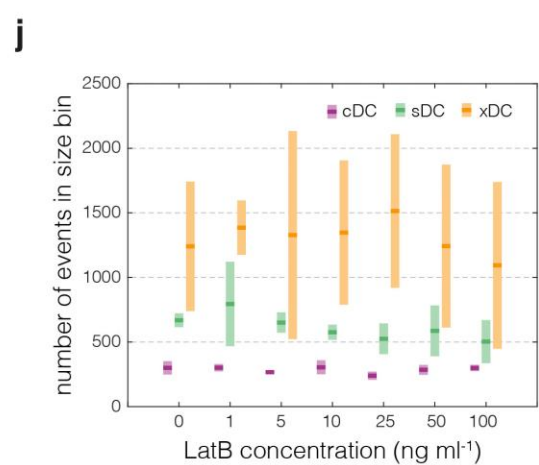
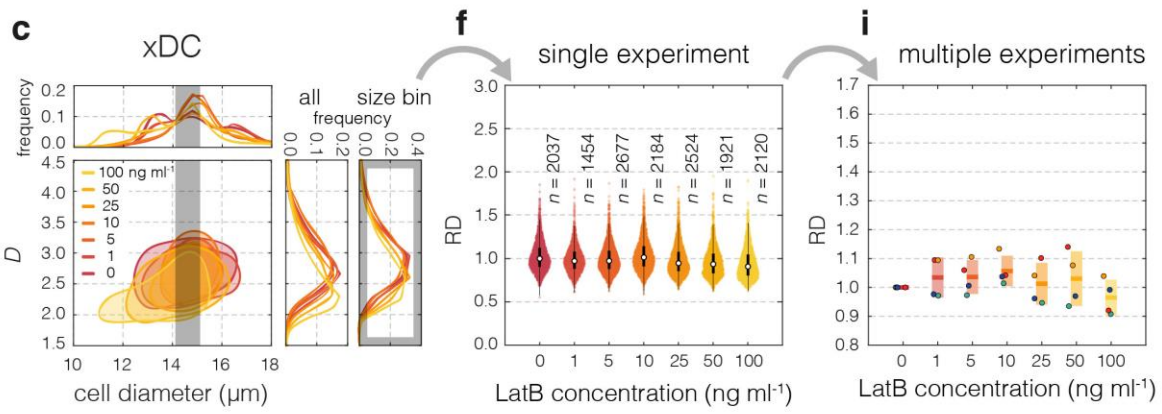
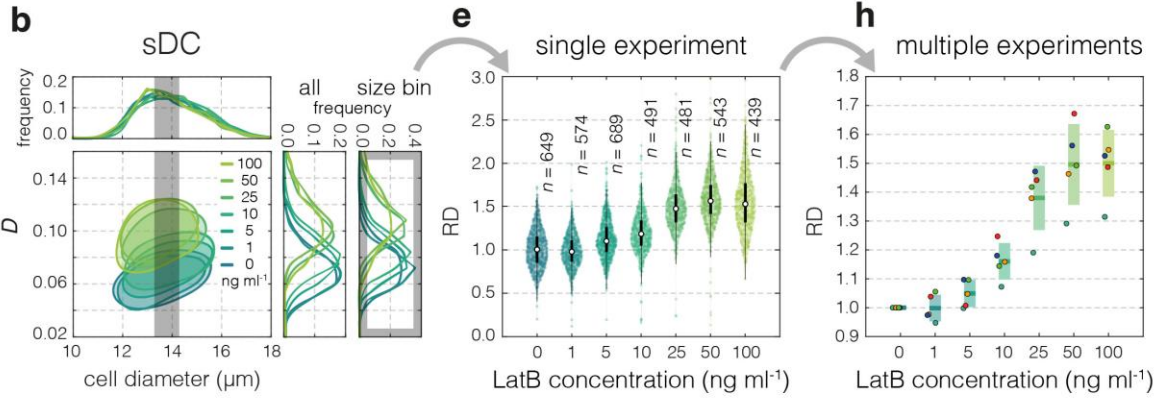
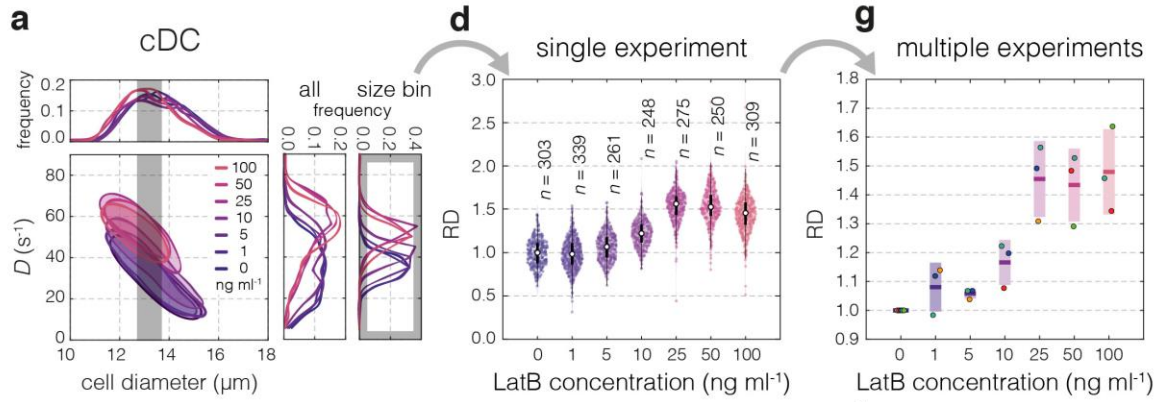
(a–c) The changes in HL60 relative deformability, RD (a), and cell diameter (b) over time after exposure to medium with altered osmolarity as measured by sDC. The experiments were performed in  $30 \times 30\text{-}\mu\text{m}$  channels at a flowrate of  $0.16 \mu\text{l s}^{-1}$ . Data points represent medians of consecutive measurements taken at different times after the exposure to altered osmolarity medium. On average 3,000 events (and not less than 1,800) were analyzed for each data point.



**Supplementary Figure 5**

**Fitting of the relation between osmolarity and relative deformability for hyperosmotic shock data.**

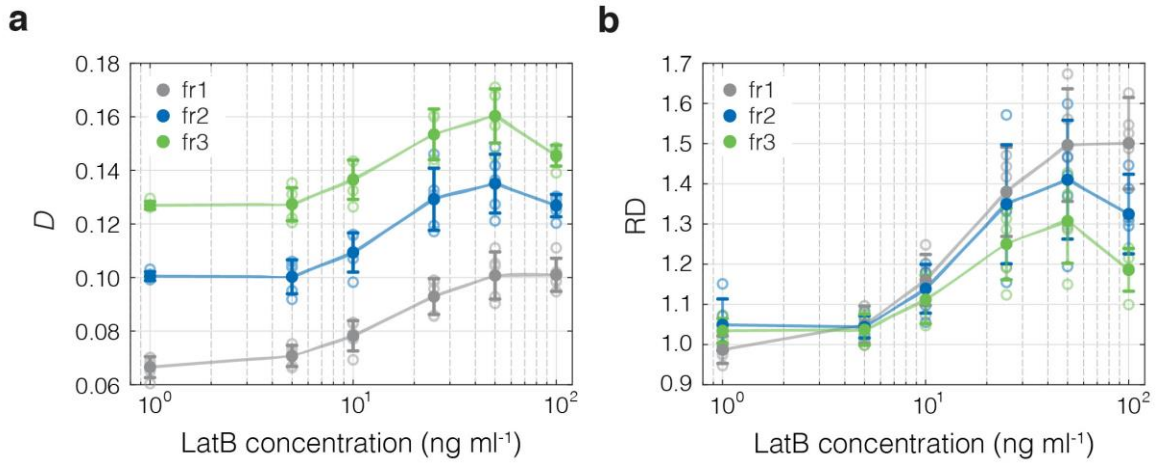
(a-c) Exponential (red), power law (green) and linear (blue) fits to relative deformability, RD, vs osmolarity data obtained with cDC (a), sDC (b) and xDC (c). Data points in a-c represent means of medians of multiple experimental replicates ( $n = 3, 4,$  and  $4,$  for cDC, sDC, and xDC, respectively), error bars represent standard deviation. (d-e) Bar graphs of mean absolute residuals (d) and Bayesian information criterion (BIC) (e), that assess the quality of different fits. Values estimated for each method, as well as mean of values for all methods ( $n = 3$ ) for given fit function, are presented. The error bars on the mean plots represent standard deviation. Mean absolute residuals give an information on how much the values predicted by the fitted function deviate from the experimental data. Lower values of residuals indicate better agreement of experimental data with proposed function. In case of BIC, lower values indicate a better fit.



## Supplementary Figure 6

### Visualization of bin selection and data processing for LatB treatment experiments.

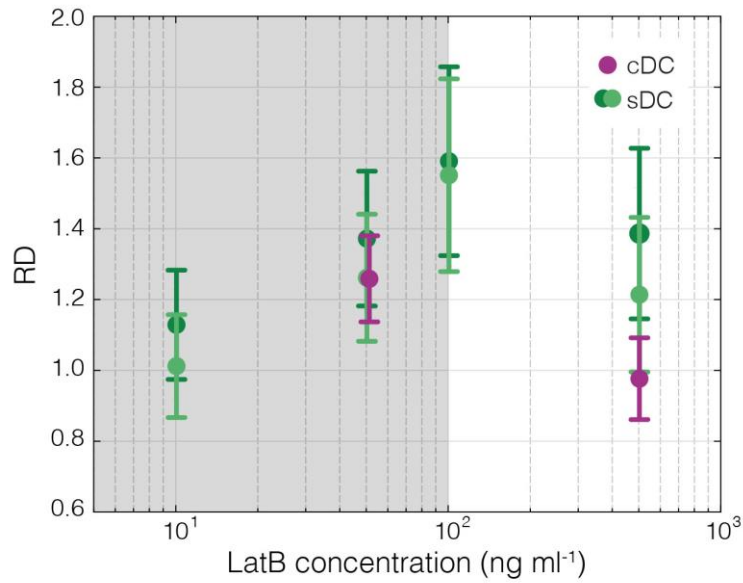
(a–c) 50%-density contour plots of deformability vs cell diameter for an exemplary experiment on HL60 cells treated with increasing concentration of LatB. The contour plots are accompanied by deformability and cell diameter histograms for cDC (a), sDC (b), and xDC (c). The most represented 1- $\mu$ m wide diameter bins used for relative deformability, RD, calculations and the corresponding deformability histograms are outlined in grey. (d–f), Jitter plots showing distribution of RD from cDC (d), sDC (e), and xDC (f) measurements for a single experiment. Boxes extend from 25th to 75th percentiles, with a dot at the median, whiskers indicate 1.5 $\times$  IQR (interquartile range) and each data point corresponds to an individual cell. (g–i), Summary of RD values obtained in all experimental series with cDC (g), sDC (h) and xDC (i). Data points correspond to medians of every experiment and conditions measured in the same experimental series are color-coded. Boxes span 2 $\times$  standard deviation with a line at the mean of all medians. (j) Number of events in the selected 1- $\mu$ m wide diameter bin for each condition and method. (k) Events selected within the 1- $\mu$ m wide diameter bin as a percentage of all events measured. In (j) and (k) the boxes span 2 $\times$  standard deviation with a line at the mean. In g–k, the statistics have been calculated for  $n = 3, 5$  and 4 independent measurement replicates, for cDC, sDC and xDC, respectively.



### Supplementary Figure 7

#### Dose-response to LatB treatment measured with sDC at three different flow rates.

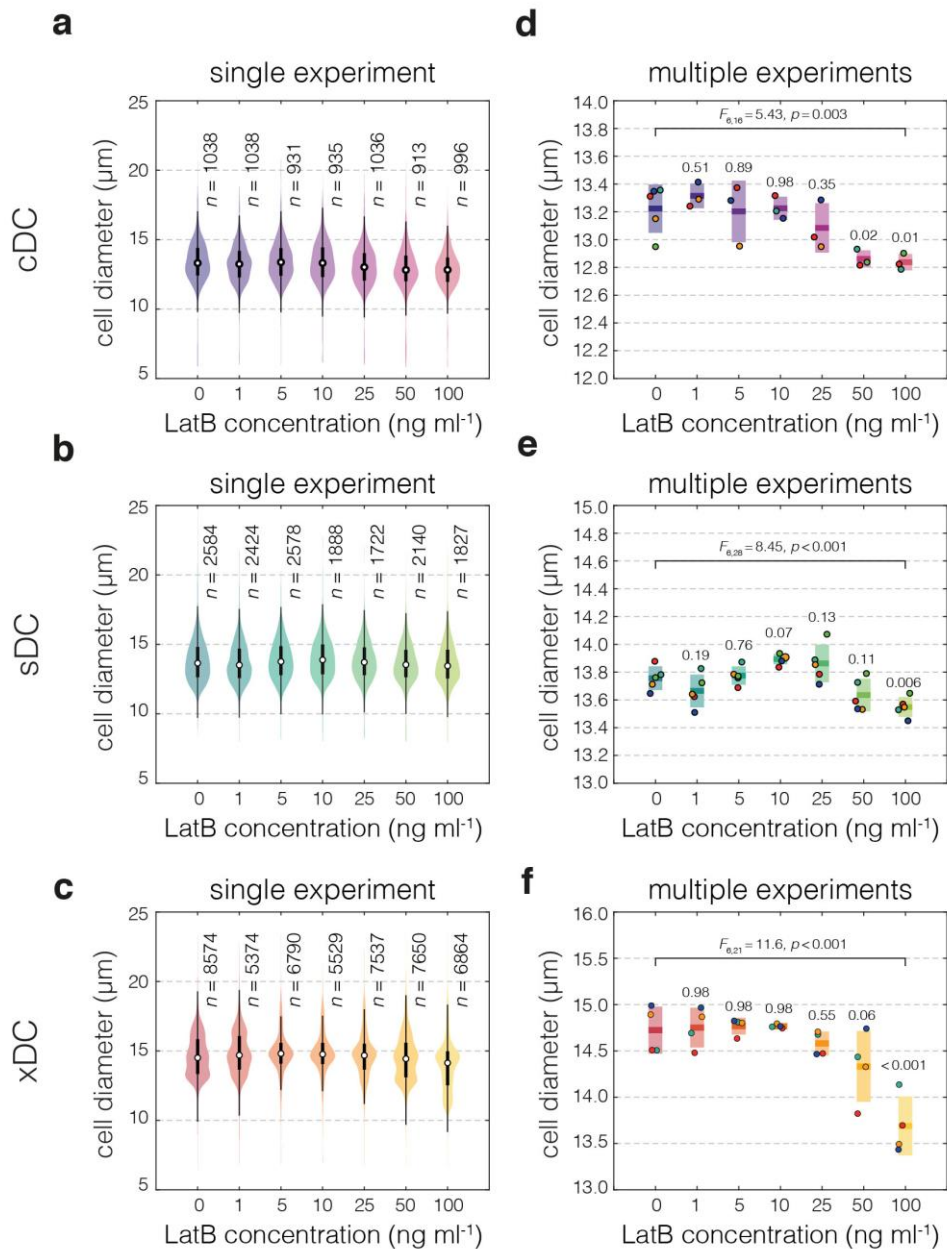
Deformability,  $D$  (a), and relative deformability, RD (b), as a function of LatB concentration at three different flowrates (fr1 = 2.4  $\mu\text{l min}^{-1}$ , fr2 = 4.8  $\mu\text{l min}^{-1}$ , and fr3 = 7.2  $\mu\text{l min}^{-1}$ ). The different flowrates are color-coded as indicated in the figure legend (fr1 – gray, fr2 – blue, fr3 – green). Open circles indicate medians of individual measurements, lines connect means of measurement replicates for each flowrate ( $n = 5$ ), error bars correspond to standard deviation of the mean distributions. Bin-selected data was used.



**Supplementary Figure 8**

**Response to high LatB concentrations measured with cDC and sDC.**

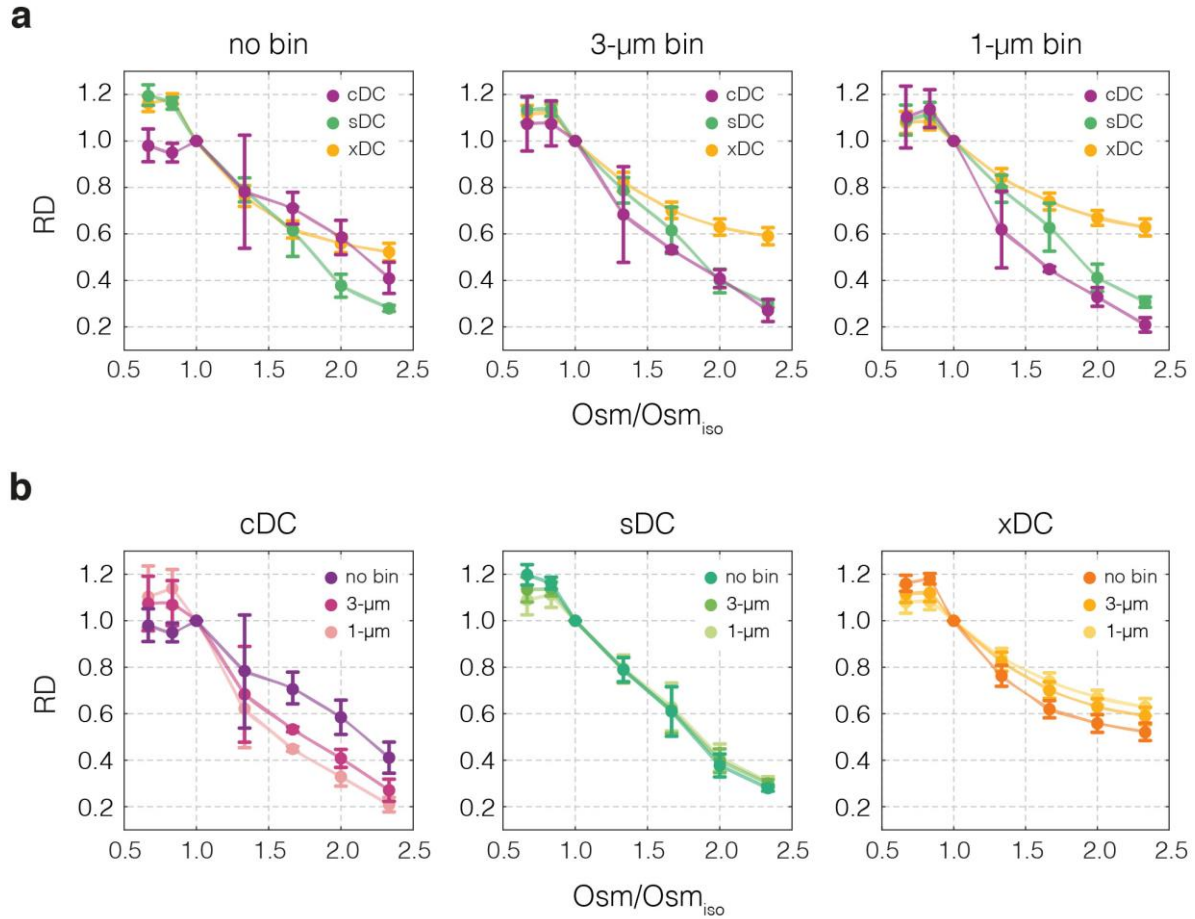
The graph shows relative deformability, RD, as a function of LatB concentration. Dots represent medians of individual measurements. Error bars represent median absolute deviation. Bin-selected data was used. One measurement series was performed using cDC (purple, from left to right  $n = 296$  and  $271$  analyzed cells in the selected size bin per data point) and two measurement series were performed using sDC (bright and dark green, from left to right  $n = 656, 537, 420, 550,$  and  $n = 734, 615, 336, 541$  analyzed cells in the selected size bin, for bright and dark green data points, respectively). The concentration range used for main analysis is shaded in gray.



**Supplementary Figure 9**

**Cell diameter of HL60 cells treated with different concentrations of LatB.**

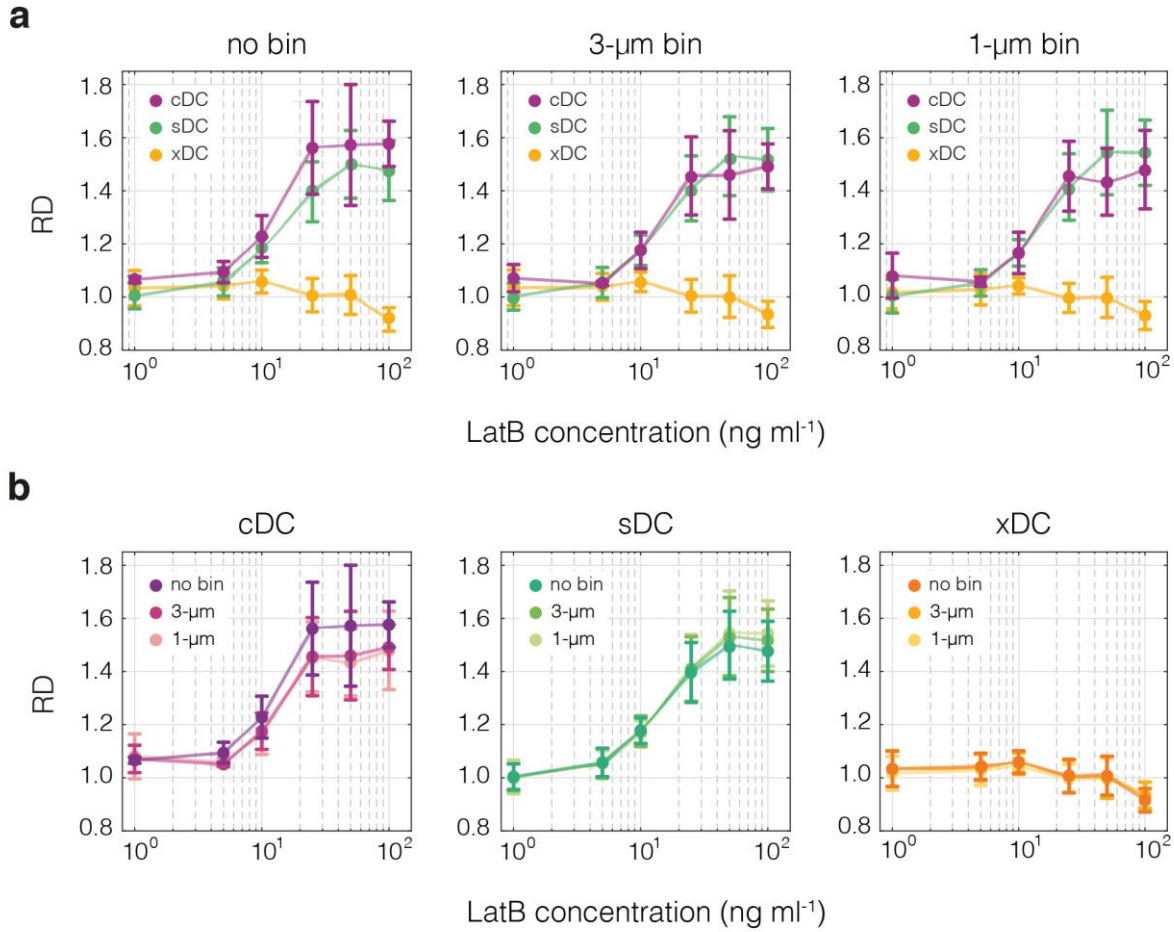
(a–c) Violin plots of cell diameter in a single experiment as measured by cDC (a), sDC (b) and xDC (c). Black boxes extend from 25th to 75th percentiles, with a dot at the median, whiskers indicate 1.5 $\times$  IQR (interquartile range). (d–f) Summary of median cell diameter values obtained in all experiment series with cDC (d), sDC (e) and xDC (f). Data points correspond to medians of individual experiments ( $n = 3, 5$  and  $4$ , for cDC, sDC and xDC, respectively). Conditions measured in same experimental series are color-coded. Boxes span 2 $\times$  standard deviation with a line at the mean of all medians. In (d–f) statistical significance of overall differences among mean cell sizes at different concentrations was tested using analysis of variance (ANOVA) and its result is shown on top of the horizontal line overarching all conditions. The  $P$  values reported above each box come from comparison of the given treatment to the control condition obtained through post-hoc analysis using pairwise two-sided  $t$ -tests for multiple comparisons with Benjamin-Hochberg  $P$ -value adjustment.



**Supplementary Figure 10**

**The influence of size bin selection on relative deformability response to osmotic shock.**

For all three methods RD was calculated for either all data, 3- $\mu$ m wide cell diameter bin or 1- $\mu$ m wide cell diameter bin. For the ease of comparison, the data is grouped based on binning strategy and all three methods are plotted together (**a**), or the data is grouped by method and all binning strategies are compared (**b**). The lines connect the data points representing means of medians from measurement replicates ( $n = 3, 4, \text{ and } 4$ , for cDC, sDC, and xDC, respectively). Error bars present the standard deviation of the medians.



**Supplementary Figure 11**

**The influence of size bin selection on relative deformability response to LatB treatment.**

For all three methods RD was calculated for either all data, 3- $\mu$ m wide cell diameter bin or 1- $\mu$ m wide cell diameter bin. For the ease of comparison, the data is grouped based on binning strategy and all three methods are plotted together (**a**), or the data is grouped by method and all binning strategies are compared (**b**). The lines connect the data points representing means of medians from measurement replicates ( $n = 3, 5, \text{ and } 4$ , for cDC, sDC, and xDC, respectively). Error bars present the standard deviation of the medians.

## Supplementary Tables

**Supplementary Table 1|** The decay constants,  $\lambda$ , for the exponential curve fit to the relative deformability versus normalized osmolarity data for hyperosmotic shock obtained with cDC, sDC, and xDC. Fits were performed on medians from  $n = 3, 4,$  and  $4$  independent experiments, for cDC, sDC, and xDC, respectively. The fitted  $\lambda$  values are reported together with 95% confidence intervals, CI, and associated  $p$ -values from two-sided  $t$ -tests for this parameter.

	cDC	sDC	xDC
$\lambda$	1.206 95% CI [1.065, 1.366] $t(16) = 17.26$ $p = 9.14 \times 10^{-12}$	0.780 95% CI [0.695, 0.873] $t(19) = 18.14$ $p = 1.86 \times 10^{-13}$	0.397 95% CI [0.363, 0.433] $t(19) = 24.02$ $p = 1.12 \times 10^{-15}$

**Supplementary Table 2** | Fit parameters for the four-parameter log-logistic regression fit to the relative deformability versus LatB concentration data obtained with cDC, sDC, and xDC. Fits were performed on medians from  $n = 3, 5,$  and 4 independent experiments, for cDC, sDC, and xDC, respectively. The fitted values are reported together with 95% confidence intervals, CI, and associated  $p$ -values from two-sided  $t$ -tests for each parameter.

	cDC	sDC	xDC
<b>b (slope)</b>	-4.47 ml ng <sup>-1</sup> 95% CI [-14.13, 5.18] $t(19) = -0.97$ $p = 0.34$	-2.06 ml ng <sup>-1</sup> 95% CI [-3.20, -0.94] $t(31) = -3.74$ $p = 7.57 \times 10^{-4}$	8.71 ml ng <sup>-1</sup> 95% CI [-72.57, 89.99] $t(24) = 0.22$ $p = 0.83$
<b>c (lower limit)</b>	1.04 95% CI [0.97, 1.10] $t(19) = 35.31$ $p < 2.20 \times 10^{-16}$	1.00 95% CI [0.95, 1.05] $t(31) = 38.13$ $p < 2.20 \times 10^{-16}$	0.96 95% CI [0.54, 1.38] $t(24) = 4.69$ $p = 9.03 \times 10^{-5}$
<b>d (upper limit)</b>	1.46 95% CI [1.38, 1.53] $t(19) = 39.71$ $p < 2.20 \times 10^{-16}$	1.52 95% CI [1.44, 1.60] $t(31) = 37.73$ $p < 2.20 \times 10^{-16}$	1.03 95% CI [1.00, 1.06] $t(24) = 77.72$ $p < 2.20 \times 10^{-16}$
<b>e (EC<sub>50</sub>)</b>	11.92 ng ml <sup>-1</sup> , 95% CI [6.82, 17.01] $t(19) = 4.90$ $p = 9.93 \times 10^{-5}$	14.85 ng ml <sup>-1</sup> , 95% CI [9.62, 20.07] $t(31) = 5.80$ $p < 2.20 \times 10^{-16}$	78.24 ng ml <sup>-1</sup> 95% CI [-273.0, 430] $t(24) = 0.46$ $p = 0.65$

**Supplementary Table 3|** Demonstrated applications of deformability cytometry methodologies. Summary of studies employing different types of deformability cytometry to investigate various processes in cell lines and in primary tissue samples.

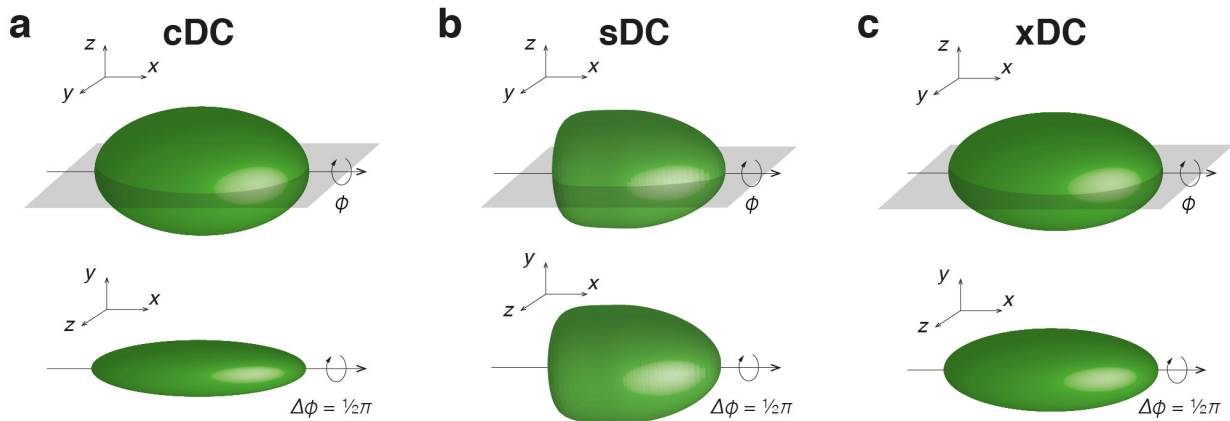
method	demonstrated biological applications
cDC	cytoskeleton perturbations <sup>1-6</sup> , chromatin reorganization <sup>4</sup> , nuclear envelope alteration <sup>4,7</sup> , inflammation mediation <sup>2</sup> , leukostasis <sup>2</sup> , cancer cell discrimination <sup>5,8</sup> , cancer cell invasion potential <sup>8</sup> , endothelial-mesenchymal transition <sup>9</sup> , osmotic stress <sup>6</sup> , protein synthesis inhibition <sup>6</sup> , cell cycle progression <sup>6</sup> , neutrophil differentiation <sup>7</sup> , oxidative damage of erythrocytes <sup>10</sup> , circulating tumor cells and blood cells discrimination <sup>9,11</sup>
sDC	cytoskeleton perturbations <sup>12-14</sup> , cell cycle progression <sup>12,15</sup> , blood cell type discrimination <sup>12,16,17</sup> , cancer malignancy <sup>14,18</sup> , erythrocyte pathologies <sup>16,19</sup> , leukocyte activation <sup>16,20,21</sup> , leukemia subtypes discrimination <sup>16</sup> , stem cell differentiation <sup>22-24</sup> , characterization of hematopoietic stem and progenitor cells <sup>25</sup> , characterization of rod photoreceptors <sup>26</sup> , yeast dormancy <sup>27</sup> , viral infection of a human cell line <sup>28</sup> , ability to pass through microcirculation <sup>29</sup>
xDC	cytoskeleton perturbation (at low probing rates) <sup>30,31</sup> , chromatin reorganization <sup>32</sup> , nuclear envelope alteration <sup>32</sup> , stem cell differentiation <sup>32-34</sup> , characterization of blood cells <sup>9</sup> and cells in pleural fluids <sup>33,35</sup> , cancer malignancy <sup>35</sup> , leukocyte activation <sup>33,36</sup> , heat-treated erythrocytes <sup>37</sup>

# Supplementary Note 1

## Estimation of Stress and Strain

### Rotational Symmetry of Deformed Cells

During a microfluidic deformation experiment, a spherical cell adapts a three-dimensional deformed shape: a prolate ellipsoid in case of cDC and xDC, and a bullet-like shape in case of sDC (**Supplementary Figure N1.1**). Depending on the geometry of the microfluidic system used, the obtained shape can be rotationally symmetric with respect to the angle  $\phi$  about the rotation axis  $x$  aligned with the longest shape dimension, or rotationally asymmetric. In case of cDC, the measurement channels used were  $6\ \mu\text{m}$  wide and  $15\ \mu\text{m}$  high which resulted in a deformation into a rotationally asymmetric ellipsoid (**Supplementary Figure N1.1a**). sDC channels had a square cross-section of  $20 \times 20\ \mu\text{m}$  resulting in a rotationally symmetric bullet-like shape (**Supplementary Figure N1.1b**). In xDC, the channels were  $60\ \mu\text{m}$  wide and  $30\ \mu\text{m}$  high. The extensional flow comes from both sides along the  $y$ -axis and exits the cross-junction towards the  $x$ -direction causing the cells to compress in  $y$ , and extend in  $x$  and  $z$  in an asymmetric way. This resulted in an ellipsoid that was not rotationally symmetric about the  $x$  axis (**Supplementary Figure N1.1c**).



**Supplementary Figure N1.1| The 3D shapes obtained during microfluidic deformation of spherical objects and their rotational views.** (a–c) 3D projections of shapes obtained during cDC (a), sDC (b) and xDC (c) measurements presented from two rotational angles  $\phi$ . The  $xyz$ -directions are given for reference in the upper left corner of each image. The gray transparencies in the upper row indicate  $xy$ -plane.

## Strain Estimation

We define strain,  $\varepsilon$ , experienced by the cell as a deviation of the local cell radius,  $r$ , from the radius of an undeformed cell,  $r_0$ , along the polar angle  $\theta$  within a plane of interest at a given rotation angle  $\phi$  about the rotation axis  $x$  aligned with the longest shape dimension (as depicted in **Supplementary Figure N1.1**):

$$\varepsilon(\theta, \phi) = \frac{r(\theta, \phi) - r_0}{r_0}. \quad (1)$$

The local strains in  $xy$ -plane,  $\varepsilon_{xy}$ , and  $xz$ -plane,  $\varepsilon_{xz}$ , can be formalized as follows

$$\varepsilon_{xy}(\theta) = \varepsilon(\theta, 0), \quad (2)$$

$$\varepsilon_{xz}(\theta) = \varepsilon\left(\theta, \frac{\pi}{2}\right). \quad (3)$$

The maximum absolute strain experienced by the cell,  $\varepsilon_{\max}$ , is defined as

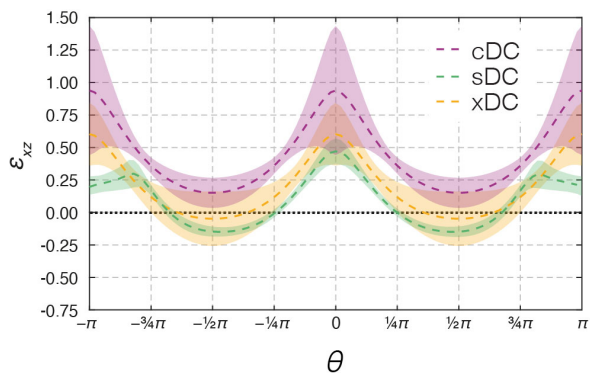
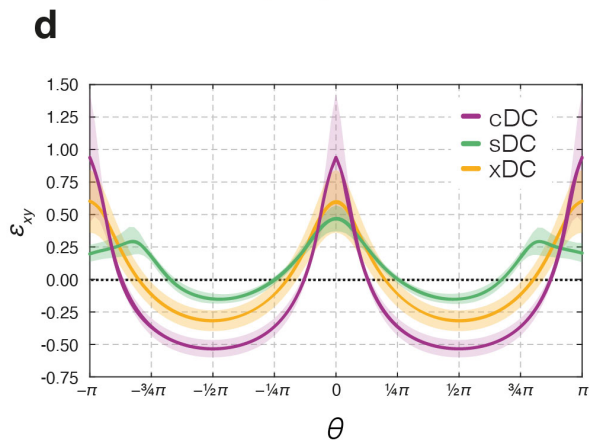
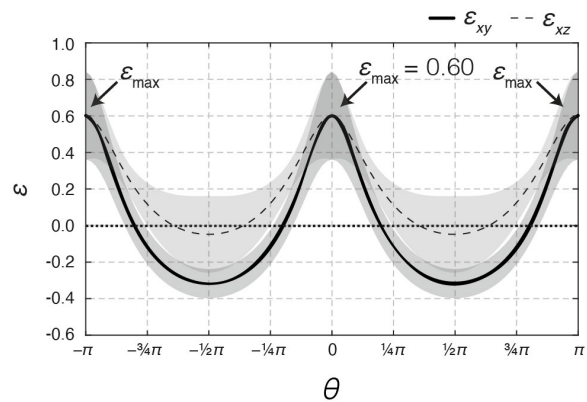
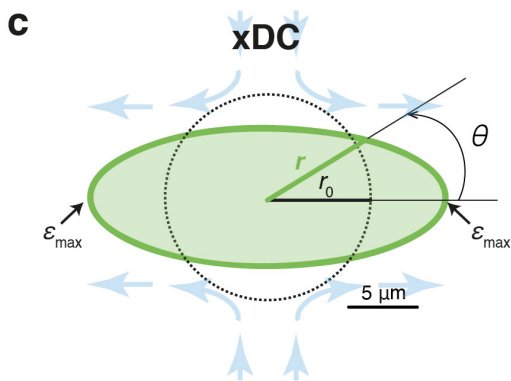
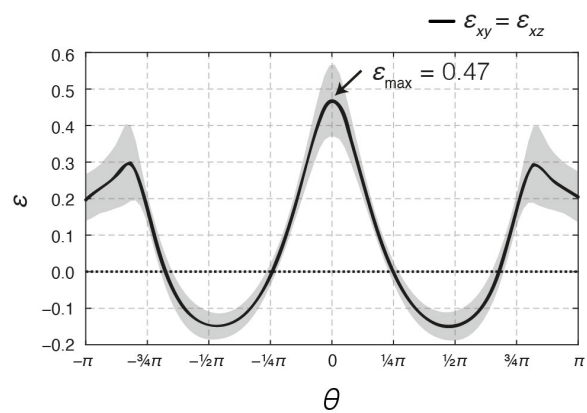
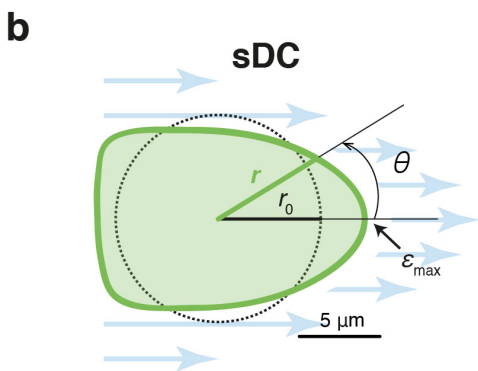
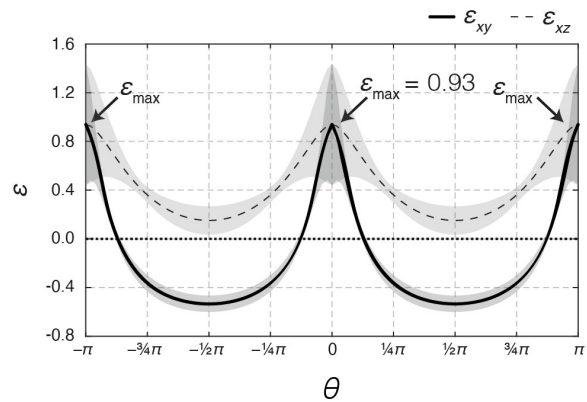
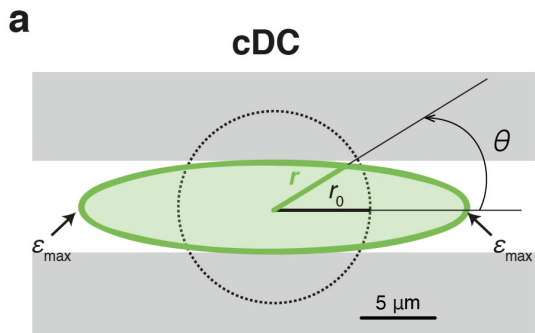
$$\varepsilon_{\max} = \max(|\varepsilon(\theta, \phi)|), \quad (4)$$

while the mean absolute strain,  $\bar{\varepsilon}$ , experienced over all polar angles  $\theta \in (-\pi, \pi)$  at every rotation angle  $\phi \in (-\pi, \pi)$  can be denoted as

$$\bar{\varepsilon} = \langle |\varepsilon(\theta, \phi)| \rangle. \quad (5)$$

For cDC,  $r_0$  is estimated for each cell from the measured cell volume as described in Methods section, and  $r(\theta, \phi)$  is calculated assuming volume conservation and a deformation into an ellipsoid with the maximum principal axes length in  $y$  and  $z$  determined by the width (6  $\mu\text{m}$ ) and height (15  $\mu\text{m}$ ) of the microconstriction, respectively. The graphical representation of the cell deformation in  $xy$ -plane together with the mean local strain estimates in  $xy$ - and in  $xz$ -planes are presented in **Supplementary Figure N1.2a**. The maximum absolute strain,  $\varepsilon_{\max}$ , for an cDC measurement on untreated HL60 cells was located at the ellipse tip along the major axis and amounted to 92%, while the average absolute strain,  $\bar{\varepsilon}$ , amounted to 37%.

For sDC,  $r_0$  is estimated for each cell assuming a sphere of volume equivalent to the volume calculated by rotating a bullet-shaped contour of deformed cell around its symmetry axis.  $r(\theta, \phi)$  represents the distance of the fitted contour to the shape's center of mass. The graphical representation of the cell deformation in the imaging plane  $xy$  as well as mean local strain estimates  $\varepsilon_{xy}(\theta)$  and  $\varepsilon_{xz}(\theta)$  are presented in **Supplementary Figure N1.2b**. The maximum absolute strain,  $\varepsilon_{\max}$ , for an sDC measurement on untreated HL60 cells is located at the tip of bullet-like shape and amounted to 47%, while the mean absolute strain,  $\bar{\varepsilon}$ , amounted to 17%.



**Supplementary Figure N1.2| Radial representation of local strain experienced by untreated HL60 cells during microfluidic deformation experiments.** (a–c) A graphical representation of undeformed and deformed sphere cross-section in the  $xy$ -plane together with local strain estimate in  $xy$ - and  $xz$ -planes along the polar angle  $\theta$  for cDC (a), sDC (b), and xDC (c). (d) An overlay of local strain in  $xy$ - (left-hand side) and  $xz$ -planes (right-hand side) for all three methods. For all plots, lines represent means over  $n = 1,428, 928, \text{ and } 6,157$  events for cDC, sDC and xDC, respectively, gathered in one representative experiment on untreated HL60 cells. Shaded areas represent standard deviations.

For xDC,  $r_0$  is specified for each cell based on the cell diameter estimated from undeformed cell images, and  $r(\theta, \phi)$  is calculated assuming volume conservation and a deformation into an ellipsoid with the experimentally determined major and minor axes in the  $xy$ -plane ( $a$  and  $b$  in Figure 1c, respectively). The graphical representation of the cell deformation in the imaging plane  $xy$  as well as mean local strain estimates  $\varepsilon_{xy}(\theta)$  and  $\varepsilon_{xz}(\theta)$  are presented in **Supplementary Figure N1.2c**. The maximum absolute strain,  $\varepsilon_{max}$ , for a xDC measurement on untreated HL60 cells was located at the ellipse tip along the major axis and amounted to 60%, while the mean absolute strain,  $\bar{\varepsilon}$ , amounted to 24%.

An overlay of  $\varepsilon_{xy}(\theta)$  and  $\varepsilon_{xz}(\theta)$  for all three methods is depicted in **Supplementary Figure N1.2d**.

### Strain Rate Estimation

The strain rate is calculated for the individual methods according to the formula

$$\dot{\varepsilon} = \frac{d\varepsilon}{dt} = \frac{\bar{\varepsilon}}{\tau}, \quad (6)$$

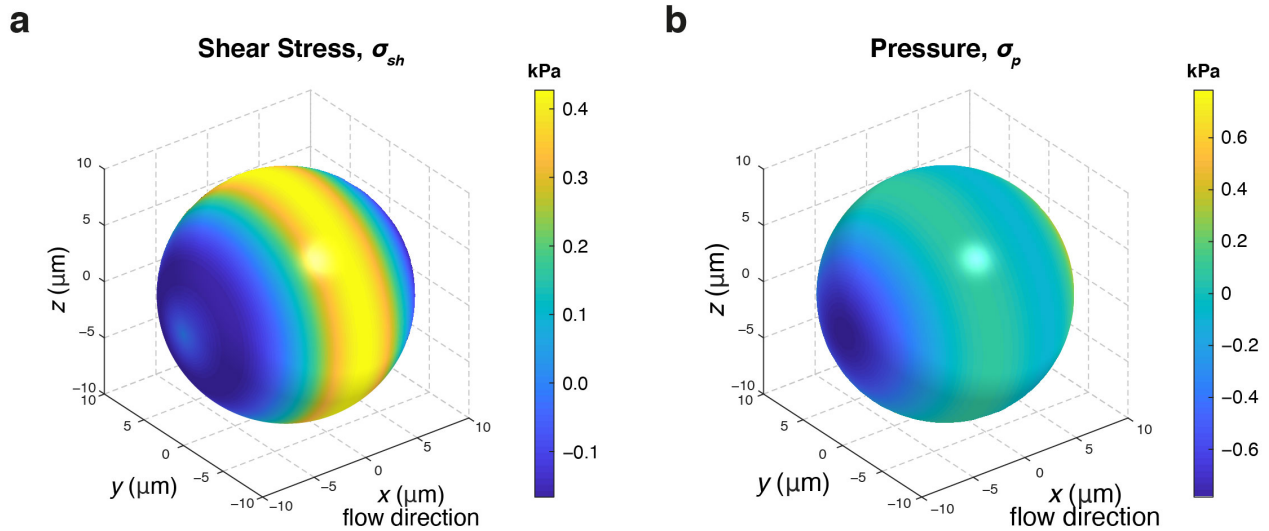
where  $\bar{\varepsilon}$  is the mean absolute strain defined in Equation (5) and  $\tau$  is the characteristic timescale of the measurement or, in other words, the time in which the cell is deformed, and is specified for each method in **Table 1**.

### Stress Estimation

The stress applied to cells passing through the microconstriction in an cDC measurement can reach a maximal value corresponding to the total applied pressure differential that drives the fluid flow in the system set to 1 kPa. This stress is applied providing that the cell fills the entire cross-section of the constriction. In reality, there are gaps between the cell and channel walls. The expected total applied stress is therefore close to, but below, 1 kPa.

There are two types of stresses acting on a cell during an sDC experiment: hydrodynamic shear stress,  $\sigma_{sh}$ , arising from velocity gradient inside the channel and acting tangentially on the cell surface, and hydrodynamic pressure,  $\sigma_p$ , which arises from pressure gradients and acts in the direction perpendicular to the cell surface. The magnitude of these stresses can be derived analytically for a case of a channel with circular cross-section using a flow-field calculated with stream function approach as previously described<sup>38</sup>. The calculations for the channel with circular cross-section were shown to deliver a good approximation of the stresses acting on the cell in a square channel of corresponding dimensions<sup>38</sup>. The results of the estimations for the parameters used during sDC experiments in our study are show in **Supplementary Figure N1.3**. The peak shear stress acting

on the cell surface amounts to roughly 0.43 kPa, and the peak hydrodynamic pressure to 0.78 kPa. Therefore, we can conclude that the deformation-relevant peak stresses in sDC are on the order of 1 kPa.



**Supplementary Figure N1.3| Analytical estimation of surface stresses acting on an undeformed sphere passing through a circular channel approximating an sDC experiment. (a–b)** A map of hydrodynamic shear stress (a) and hydrodynamic pressure (b) on a surface of a sphere of radius  $6.5 \mu\text{m}$  passing through a cylindrical channel with a diameter of  $20 \mu\text{m}$  at a flowrate of  $0.04 \mu\text{l s}^{-1}$  and medium viscosity of  $5.7 \text{ mPa s}$ , corresponding to the shear-adjusted viscosity of the used measurement buffer<sup>39</sup>.

In xDC, there are two type of forces acting on a cell in the extensional-flow region, the drag force and the shear force, with the drag force being three order of magnitudes bigger than the shear force<sup>33</sup>. The drag force acting on a cell is estimated to exceed  $1 \mu\text{N}$ <sup>33</sup>, therefore the corresponding estimated stress acting on a cell with a diameter of  $15 \mu\text{m}$  would amount to values exceeding  $5.7 \text{ kPa}$ .

## References

1. Byun, S. *et al.* Characterizing deformability and surface friction of cancer cells. *Proc. Natl. Acad. Sci. U. S. A.* **110**, 7580–5 (2013).
2. Rosenbluth, M. J., Lam, W. A. & Fletcher, D. A. Analyzing cell mechanics in hematologic diseases with microfluidic biophysical flow cytometry. *Lab Chip* **8**, 1062–1070 (2008).
3. Adamo, A. *et al.* Microfluidics-based assessment of cell deformability. *Anal. Chem.* **84**, 6438–6443 (2012).
4. Lange, J. R. *et al.* Microconstriction Arrays for High-Throughput Quantitative Measurements of Cell Mechanical Properties. *Biophys. J.* **109**, 26–34 (2015).
5. Nyberg, K. D. *et al.* Quantitative Deformability Cytometry: Rapid, Calibrated Measurements of Cell Mechanical Properties. *Biophys. J.* **113**, 1574–1584 (2017).
6. Byun, S., Hecht, V. C. & Manalis, S. R. Characterizing Cellular Biophysical Responses to Stress by Relating Density, Deformability, and Size. *Biophys. J.* **109**, 1565–1573 (2015).
7. Rowat, A. C. *et al.* Nuclear envelope composition determines the ability of neutrophil-type cells to passage through micron-scale constrictions. *J. Biol. Chem.* **288**, 8610–8618 (2013).
8. Nyberg, K. D. *et al.* Predicting cancer cell invasion by single-cell physical phenotyping. *Integr. Biol.* **10**, 218–231 (2018).
9. Shaw Bagnall, J. *et al.* Deformability of Tumor Cells versus Blood Cells. *Sci. Rep.* **5**, 18542 (2016).
10. Kwan, J. M., Guo, Q., Kyluik-Price, D. L., Ma, H. & Scott, M. D. Microfluidic analysis of cellular deformability of normal and oxidatively damaged red blood cells. *Am. J. Hematol.* **88**, 682–689 (2013).
11. Shaw Bagnall, J. *et al.* Deformability-based cell selection with downstream immunofluorescence analysis. *Integr. Biol.* **8**, 654–664 (2016).
12. Otto, O. *et al.* Real-time deformability cytometry: on-the-fly cell mechanical phenotyping. *Nat. Methods* **12**, 199–202 (2015).
13. Golfier, S. *et al.* High-throughput cell mechanical phenotyping for label-free titration assays of cytoskeletal modifications. *Cytoskeleton* **74**, 283–296 (2017).
14. Ahmmed, S. M. *et al.* Multi-sample deformability cytometry of cancer cells. *APL Bioeng.* **2**, 032002 (2018).
15. Rosendahl, P. *et al.* Real-time fluorescence and deformability cytometry. *Nat. Methods* **15**, 355 (2018).
16. Toepfner, N. *et al.* Detection of human disease conditions by single-cell morpho-rheological phenotyping of blood. *Elife* **7**, e29213 (2018).
17. Fregin, B. *et al.* High-throughput single-cell rheology in complex samples by dynamic real-time deformability cytometry. *Nat. Commun.* **10**, 415 (2019).
18. Tavares, S. *et al.* Actin stress fiber organization promotes cell stiffening and proliferation of pre-invasive breast cancer cells. *Nat. Commun.* **8**, 15237 (2017).
19. Koch, M. *et al.* *Plasmodium falciparum* erythrocyte-binding antigen 175 triggers a biophysical change in the red blood cell that facilitates invasion. *Proc. Natl. Acad. Sci.* **114**, 4225–4230 (2017).

20. Steffen, S. *et al.* Toll-Like Receptor-Mediated Upregulation of CXCL16 in Psoriasis Orchestrates Neutrophil Activation. *J. Invest. Dermatol.* **138**, 344–354 (2018).
21. Bashant, K. R. *et al.* Real-time deformability cytometry reveals sequential contraction and expansion during neutrophil priming. *J. Leukoc. Biol.* 1–11 (2019).
22. Urbanska, M. *et al.* Single-cell mechanical phenotype is an intrinsic marker of reprogramming and differentiation along the mouse neural lineage. *Development* 4313–4321 (2017).
23. Xavier, M. *et al.* Mechanical phenotyping of primary human skeletal stem cells in heterogeneous populations by real-time deformability cytometry. *Integr. Biol.* **8**, 616–623 (2016).
24. Kräter, M. *et al.* Cell-derived Bone marrow-mimetics induce erythroid lineage commitment of hematopoietic stem and progenitor cells ex-vivo. *Matters* **3**, e201709000004 (2017).
25. Jacobi, A. *et al.* Analysis of Biomechanical Properties of Hematopoietic Stem and Progenitor Cells Using Real-Time Fluorescence and Deformability Cytometry. in *Methods in Molecular Biology* vol. 2017 135–148 (Humana Press Inc., 2019).
26. Santos-Ferreira, T. *et al.* Morpho-Rheological Fingerprinting of Rod Photoreceptors Using Real-Time Deformability Cytometry. *Cytom. Part A* **95**, 1145–1157 (2019).
27. Munder, M. C. *et al.* A pH-driven transition of the cytoplasm from a fluid- to a solid-like state promotes entry into dormancy. *Elife* **5**, (2016).
28. Kräter, M. *et al.* Alterations in Cell Mechanics by Actin Cytoskeletal Changes Correlate with Strain-Specific Rubella Virus Phenotypes for Cell Migration and Induction of Apoptosis. *Cells* **7**, 136 (2018).
29. Tietze, S. *et al.* Spheroid Culture of Mesenchymal Stromal Cells Results in Morphorheological Properties Appropriate for Improved Microcirculation. *Adv. Sci.* 1802104 (2019) doi:10.1002/advs.201802104.
30. Guillou, L. *et al.* Measuring Cell Viscoelastic Properties Using a Microfluidic Extensional Flow Device. *Biophys. J.* **111**, 2039–2050 (2016).
31. Armistead, F. J., De Pablo, J. G., Gadêlha, H., Peyman, S. A. & Evans, S. D. Cells Under Stress: An Inertial-Shear Microfluidic Determination Of Cell Behaviour. *Biophys. J.* (2019).
32. Masaeli, M. *et al.* Multiparameter mechanical and morphometric screening of cells. *Sci. Rep.* **6**, 37863 (2016).
33. Gossett, D. R. *et al.* Hydrodynamic stretching of single cells for large population mechanical phenotyping. *Proc. Natl. Acad. Sci.* **109**, 7630–7635 (2012).
34. Lin, J. *et al.* High-throughput physical phenotyping of cell differentiation. *Microsystems Nanoeng.* **3**, 17013 (2017).
35. Tse, H. T. K. *et al.* Quantitative diagnosis of malignant pleural effusions by single-cell mechanophenotyping. *Sci. Transl. Med.* **5**, 212ra163 (2013).
36. Crawford, K. *et al.* Rapid Biophysical Analysis of Host Immune Cell Variations Associated with Sepsis. *Am. J. Respir. Crit. Care Med.* **198**, 280–282 (2018).
37. Cha, S. *et al.* Cell Stretching Measurement Utilizing Viscoelastic Particle Focusing. *Anal. Chem.* **84**, 10471–10477 (2012).

38. Mietke, A. *et al.* Extracting Cell Stiffness from Real-Time Deformability Cytometry: Theory and Experiment. *Biophys. J.* **109**, 2023–2036 (2015).
39. Herold, C. Mapping of Deformation to Apparent Young's Modulus in Real-Time Deformability Cytometry. *ArXiv* <http://arxiv.org/abs/1704.00572> (2017).